Earth and Planetary Science Letters 489 (2018) 251–257

Contents lists available at ScienceDirect

Earth and Planetary Science Letters

www.elsevier.com/locate/epsl

Evidence for {100}<011> slip in ferropericlase in Earth's lower mantle from high-pressure/high-temperature experiments

J. Immoor [a], H. Marquardt [a,*], L. Miyagi [b], F. Lin [b], S. Speziale [c], S. Merkel [d], J. Buchen [a], A. Kurnosov [a], H.-P. Liermann [e]

[a] Bayerisches Geoinstitut BGI, University of Bayreuth, 95440 Bayreuth, Germany
[b] University of Utah, 115 So. 1460 E., Salt Lake City, UT 84112-0111, USA
[c] German Research Center for Geosciences GFZ, 14473 Potsdam, Germany
[d] Univ. Lille, CNRS, INRA, ENSCL, UMR 8207 – UMET – Unité Matériaux et Transformations, F-59000 Lille, France
[e] Deutsches Elektronen-Synchrotron (DESY), 22607 Hamburg, Germany

ARTICLE INFO

Article history:
Received 24 November 2017
Received in revised form 19 February 2018
Accepted 28 February 2018
Available online xxxx
Editor: J. Brodholt

Keywords:
ferropericlase
rheology
lower mantle
seismic anisotropy
large low shear velocity provinces

ABSTRACT

Seismic anisotropy in Earth's lowermost mantle, resulting from Crystallographic Preferred Orientation (CPO) of elastically anisotropic minerals, is among the most promising observables to map mantle flow patterns. A quantitative interpretation, however, is hampered by the limited understanding of CPO development in lower mantle minerals at simultaneously high pressures and temperatures. Here, we experimentally determine CPO formation in ferropericlase, one of the elastically most anisotropic deep mantle phases, at pressures of the lower mantle and temperatures of up to 1400 K using a novel experimental setup. Our data reveal a significant contribution of slip on {100} to ferropericlase CPO in the deep lower mantle, contradicting previous inferences based on experimental work at lower mantle pressures but room temperature. We use our results along with a geodynamic model to show that deformed ferropericlase produces strong shear wave anisotropy in the lowermost mantle, where horizontally polarized shear waves are faster than vertically polarized shear waves, consistent with seismic observations. We find that ferropericlase alone can produce the observed seismic shear wave splitting in D″ in regions of downwelling, which may be further enhanced by post-perovskite. Our model further shows that the interplay between ferropericlase (causing $V_{SH} > V_{SV}$) and bridgmanite (causing $V_{SV} > V_{SH}$) CPO can produce a more complex anisotropy patterns as observed in regions of upwelling at the margin of the African Large Low Shear Velocity Province.

1. Introduction

Seismic shear wave splitting is a key observable in the D″ region at the base of the mantle. Anisotropy is observed both in regions where slabs might impinge on the core–mantle boundary (CMB) (Lay et al., 1998; Garnero et al., 2004; Panning and Romanowicz, 2004) and adjacent to ultra-low velocity zones at the margins of the African Large Low Shear Wave Velocity Province (LLSVP) (Cottaar and Romanowicz, 2013; Lynner and Long, 2014). These seismic observations are among the most promising features to map mantle flow patterns and link them to surface processes, provided that the underlying principles are understood (Romanowicz and Wenk, 2017). It is usually assumed that seismic anisotropy is the expression of Crystallographic Preferred Orientation (CPO) of elastically anisotropic lower mantle minerals as a result of deformation by dislocation creep (Merkel et al., 2007; Miyagi et al., 2010; Nowacki et al., 2011; Romanowicz and Wenk, 2017).

Several past studies combined mineral-physics derived information on the elastic anisotropy as well as the CPO-formation in lower mantle phases with both 2D (Wenk et al., 2006, 2011) and 3D (Walker et al., 2011; Cottaar et al., 2014) flow field models in attempts to explain lowermost mantle seismic anisotropy in regions where slabs might reach the core–mantle-boundary region, with review articles by Nowacki et al. (2011), Romanowicz and Wenk (2017). Most of these previous works have focused on predicting seismic shear wave splitting that could result from CPO of post-perovskite, the most abundant phase in colder regions of the lowermost mantle. While these studies generally conclude that post-perovskite could explain seismic anisotropy in the D″ layer (Miyagi et al., 2010; Walker et al., 2011; Wenk et al., 2011; Nowacki et al., 2013), the results are still inconclusive as they

* Corresponding author.
E-mail address: Hauke.Marquardt@uni-bayreuth.de (H. Marquardt).

https://doi.org/10.1016/j.epsl.2018.02.045
0012-821X/

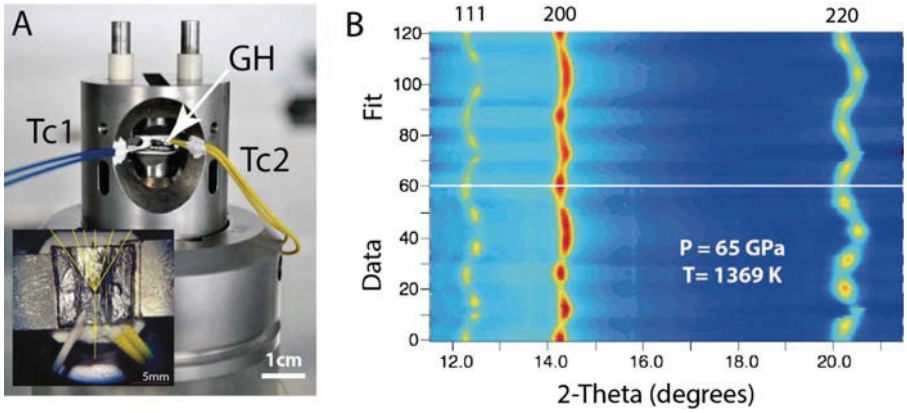

Fig. 1. Experimental setup and results. (A) Photograph of the resistive-heated DAC used in this study. GH: Graphite-heater; Tc: Thermocouple. Inset shows the lower diamond pressed into the graphite-heater and illustrates the positions of the thermocouples. (B) Diffraction data collected at simultaneous high-P/T (65 GPa, 1369 K, bottom) along with the best-fit model (top). The intensity variations along the unrolled diffraction rings are caused by ferropericlase lattice preferred orientation, the curvature is a measure of elastic lattice strains.

strongly depend on the debated dominant slip systems operating in post-perovskite at lowermost mantle conditions (Walker et al., 2011; Wenk et al., 2011) and may further be affected by transformation textures (Miyagi et al., 2010; Dobson et al., 2013; Walker et al., 2017).

Much less attention has been focused on the possibility of CPO of (Mg,Fe)O ferropericlase, the second most abundant mineral in a pyrolitic lower mantle, as the cause of seismic anisotropy. Ferropericlase is characterized by significant elastic anisotropy that steadily increases with depth and is further enhanced by the iron spin crossover (Lin et al., 2013) in the mid-lower mantle (Marquardt et al., 2009). In the Earth's lowermost mantle, the elastic anisotropy of ferropericlase is significantly larger as compared to bridgmanite or post-perovskite (Marquardt et al., 2009). This marked elastic anisotropy combined with its rheological weakness (Yamazaki et al., 2009; Marquardt and Miyagi, 2015; Girard et al., 2016) makes ferropericlase a strong candidate phase to generate seismic anisotropy in the lower mantle. The extent to which the intrinsic anisotropy of ferropericlase contributes to seismic anisotropy observed in the lowermost mantle depends on the way ferropericlase crystals orient in the flow field of the mantle. CPO development is controlled by deformation geometry and the relative activities of various available plastic deformation modes. In ferropericlase these appear to be highly sensitive to pressure, temperature (Amodeo et al., 2012) and possibly strain rate (Cordier et al., 2012). Previous work has shown that dislocation creep in (Mg,Fe)O at mantle pressures takes place by slip along <110> directions on either the {100} or the {110} planes, i.e. the slip systems {100}<011> and {110}<1–10> (Merkel et al., 2002; Lin et al., 2009; Cordier et al., 2012; Girard et al., 2012; Marquardt and Miyagi, 2015; Lin et al., 2017). The effects of lower mantle pressure and temperature conditions on the relative contribution of these two slip systems is experimentally unconstrained, hampering any reliable modeling of the contribution of ferropericlase to lower mantle seismic anisotropy. In particular, it was suggested that only slip on {100} is consistent with the seismic record in the D″ layer in the lowermost mantle (Karato, 1998), but room-pressure diamond-anvil cell work by synchrotron radial X-ray diffraction (rXRD) on polycrystalline MgO and (Mg,Fe)O concluded that slip on {110} is dominant to pressures of almost 100 GPa (Merkel et al., 2002; Lin et al., 2009). A more recent rXRD study pointed out the possibility that slip system activities might change with pressure at 300 K (based on a subtle decrease of the observed texture maximum), but could not provide evidence from CPO analysis (Marquardt and Miyagi, 2015). In contrast to diamond-anvil cell work, experimental work on polycrystalline (Mg,Fe)O at high temperatures, but low pressures, reported {100}<011> to be the dominant slip system (Stretton et al., 2001). Experimental work carried out on MgO single-crystals at temperatures between 1200 and 1473 K proposed a change of slip system activities with pressure, where {110}<1–10> slip dominates at low pressures, but slip on {100} becomes favorable at pressures beyond the ones achieved in the experiment (Girard et al., 2012). Early theoretical work provided contradictory predictions, indicating either preferred slip on {110} up to at least 100 GPa (Carrez et al., 2009), or a change of dominant slip system with pressure (Karato, 1998). Most recent modeling results of the critical resolved shear stresses (CRSS) in single-crystal MgO suggest dominant {100}<011> slip at pressures above 40–60 GPa both at 300 K and high temperatures (Amodeo et al., 2012, 2016; Cordier et al., 2012). Here, we experimentally determine slip system activities in polycrystalline $(Mg_{0.8}Fe_{0.2})O$ ferropericlase at pressures of the lower mantle and temperatures of up to about 1400 K using rXRD experiments in a resistive-heated DAC. We combine our findings with a previous geodynamic model to evaluate the contribution of ferropericlase CPO to the observed seismic anisotropy in the lowermost mantle.

2. Methods

In this work, we conducted experimental measurements of ferropericlase deformation in the graphite resistive-heated DAC. The experimental approach is outlined in section 2.1. The following section 2.2 introduces the subsequent modeling that has been performed to (a) extract slip system activities from the experimental data (EVPSC, section 2.2.1) and (b) combine these with results of a previous geodynamic model to estimate the possible contribution of ferropericlase to seismic anisotropy in the lower mantle (section 2.2.2).

2.1. Experimental procedure

2.1.1. Samples

The starting materials were finely-ground powders of $(Mg_{0.8}Fe_{0.2})O$ made from stoichiometric mixtures of reagent grade MgO and Fe_2O_3 reacted in a gas-mixing furnace at 1250 °C at an oxygen fugacity 2 log units below the fayalite–magnetite oxygen buffer. The powdered sample was loaded into the pressure chamber of a Mao–Bell-type Diamond-anvil cell (DAC).

2.1.2. Graphite-heated diamond-anvil cell (DAC)

Customised Mao–Bell-type DACs were used in our experiments employing diamond anvils with culet sizes of 200 μm and 300 μm (Fig. 1). X-ray transparent gaskets with a hole of 80 μm diameter made of either amorphous boron epoxy or cubic boron nitride

Table 1
Summary of experimental run conditions.

Name of experimental run	Tc1	Pre-compression	Pressure after heating	Peak pressure
300 K	Ambient (Marquardt and Miyagi, 2015)	–	–	96 GPa
800 K	823 K	5 GPa	4 GPa	67 GPa
1150 K	1136 K	3 GPa	6 GPa	74 GPa
1400 K	1369 K	37 GPa	21 GPa	65 GPa

were employed. The gaskets were held in place by a piece of Kapton. A resistive-heater that surrounds the diamond tips was made of two thin flexible graphite layers that are in tight contact with the diamond anvils. To allow X-rays to pass through the heater, a beampath was carved into the graphite sheets (Liermann et al., 2009). Temperature was monitored by two type-R thermocouples (see Fig. 1). The entire DAC was positioned inside a vacuum chamber designed at the Extreme Condition Beamline (ECB, P02.2) at PETRA III of the Deutsches Elektronensynchrotron (DESY) (Liermann et al., 2015). A vacuum of better then 10^{-4} mbar was maintained during heating to avoid oxidation of the cell and diamonds. The outside of the vacuum chamber was kept at low temperatures by a water-cooling system (Liermann et al., 2015).

2.1.3. Synchrotron radial X-ray diffraction experiments

The vacuum chamber was mounted on the general purpose station at the ECB and diffraction experiments were conducted using X-ray energies of either 25 or 43 keV. X-rays were focused to about 7.5 (H) by 2 (V) μm^2. Diffraction images were collected from the center of the diamond culet employing a Perkin Elmer Flat Panel 1621 Detector for 30 s. In all experimental runs, the sample was pre-compressed before heating (Table 1). Temperature at high-pressures was increased slowly (over several hours) to allow the system to equilibrate and maintain the vacuum. After reaching the target temperature, the temperature was kept constant throughout the experiment while the pressure was increased remotely using a gas-membrane system. The pressure was determined from the unit cell volume of ferropericlase using existing thermal equation of state parameters (compiled in Stixrude and Lithgow-Bertelloni, 2011). We conducted experimental runs at pressures up to 74 GPa at temperatures of about 800 K, 1150 K and 1400 K and collected diffraction images in pressure steps of 1–5 GPa to monitor the evolution of sample texture and strain (Table 1).

2.1.4. Data reduction

The collected X-ray diffraction images were sliced in steps of 5° and analyzed using the program MAUD (Lutterotti et al., 1997) generally following a previously outlined procedure (Wenk et al., 2014) (Fig. 1). The background was corrected for by using polynomial functions. The "radial diffraction in the DAC" model (Singh et al., 1998) was used to fit lattice strains in ferropericlase. The E-WIMW model which is similar to the WIMV model (Matthies and Vinel, 1982), but allows for incomplete and arbitrary pole figure coverage was employed to fit textures.

2.2. Modeling of experimental results and geophysical modeling

2.2.1. EVPSC modeling

We used an Elasto-Plastic Self-Consistent code (Wang et al., 2010; Lin et al., 2017) to model the pressure evolution of texture and lattice strains in our experiments. The modeling of the experimental data followed the procedure described before (Merkel et al., 2009) and also applied to periclase (Lin et al., 2017). Modeled lattice strains for the 1400 K experimental run are shown as an example in Fig. S1 and compared to the experimental data (Figs. 2 and 3). A second order polynomial was used to represent the pressure dependence of the CRSS (τ) and adjusted to match the experimentally observed lattice strains up to 56 GPa. In the simulation, we excluded data points that have been collected away from the center of the culet. Note that the apparent CRSS are only valid within the experimental pressure range.

No explicit strain hardening was imposed in the simulation due to elevated temperatures. Moreover, it is not possible to separate the relative effects of pressure and strain on the strengthening of the CRSS based on the present experimental data because pressure and strain increase simultaneously during compression. Strain hardening and pressure strengthening are parameterized in EVPSC using the same formalism and have the same effect. Separating the relative contribution of pressure and strain on hardening would require experimental data in which different strains are achieved for the same pressure, which is not possible with current DAC experiment. Here, we hence combined the two effects into the pressure strengthening parameters.

A stress exponent of $n = 5$ was used for all slip systems. We found that increasing or decreasing the value of the stress exponent by 1 or 2 does not significantly change the modeling results. The $\{111\}\langle 1\bar{1}0\rangle$ slip system is given a very high initial CRSS to fully suppress its activity. Different grain-interaction models (affine, secant, tangent) were tested, but resulted in comparable pressure evolutions of lattice strain and texture. The input parameters employed for the modeling of the 1400 K compression run are summarized in Table 2.

2.2.2. Large-scale modeling

To model large scale seismic anisotropy development we utilized a 2D geodynamic model that has been previously used to predict anisotropy development in a slab subducted along the D″ (McNamara and Zhong, 2005; Merkel et al., 2007; Miyagi et al., 2010). A tracer records strain and temperature history and by coupling this with the VPSC (Lebensohn and Tomé, 1994), we simulated texture development in a slab that is first subducted to the core mantle boundary (CMB), is deformed laterally across the CMB, and then begins to rise away from the CMB. We assumed that the aggregate enters the top of the D″ (~290 km above the CMB) with a random orientation distribution and that only 10% of total strain accumulated by the strain tracer is accommodated by dislocations. This allows for the additional contribution of diffusion processes (such as climb and creep) which do not generate significant CPO development. In order to show the effect of {100} slip on anisotropy development in the lowermost mantle, we assume a ratio of slip system strengths (CRSS) of 10:1 for slip on $\{110\}\langle 1\text{–}10\rangle$ and $\{100\}\langle 011\rangle$. Slip on {111} is fully suppressed. No hardening was used in the model as work hardening is unlikely to be significant at the low strain rates of the lowermost mantle. Slip on $\{100\}\langle 011\rangle$ dominates deformation along the streamline with 99 % strain accommodated on $\{100\}\langle 011\rangle$. By averaging single-crystal elastic constants of MgO (Karki et al., 1999) over the orientation distribution we calculated the aggregate elastic properties. For averaging of the elastic constants we employed the geometric mean (Matthies and Humbert, 1993) which lies close to the Hill average. Anisotropy development in bridgmanite was also modeled along the streamline in the same manner as was done for ferropericlase. We used previously published CRSS values (Miyagi

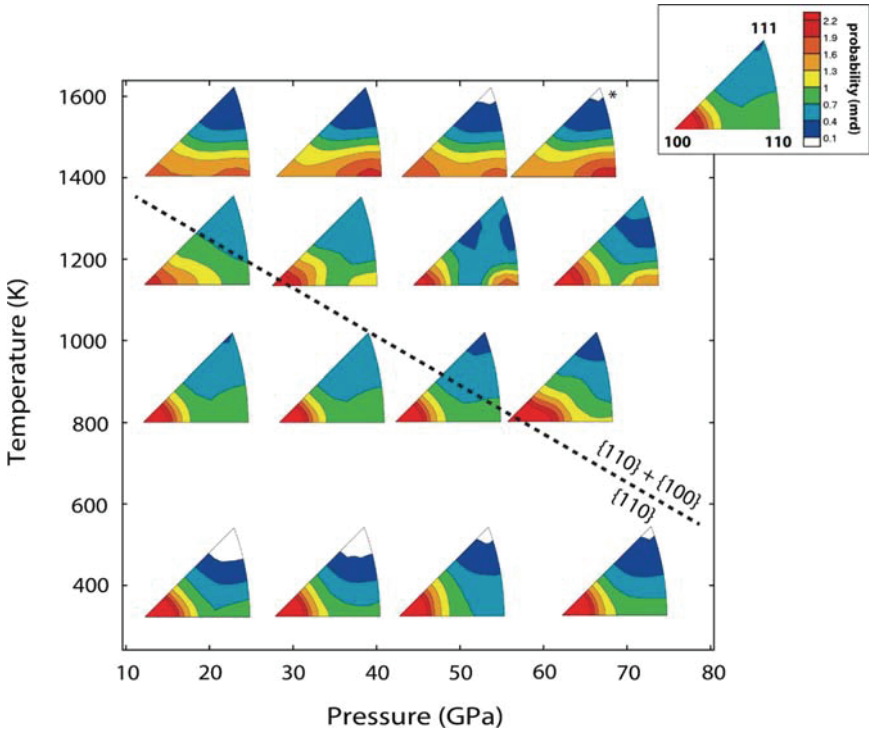

Fig. 2. Ferropericlase texture evolution observed in our experiments. Data at 300 K are from previous work (Marquardt and Miyagi, 2015) on the same sample material. The lower right corners of the IPFs are placed at the corresponding P/T-conditions. The dashed line is intended for illustration only and highlights the transition from dominant slip on {110} to a regime where slip on {110} and {100} are equally important as judged from the IPF appearances. All textures have been derived from measurements at the center of the sample, except for the point at 65 GPa and 1400 K (denoted with a star) which was collected with the beam approximately 10 µm away from the sample center. The inset shows the axes and color scale of the IPF. (For interpretation of the colors in the figure(s), the reader is referred to the web version of this article.)

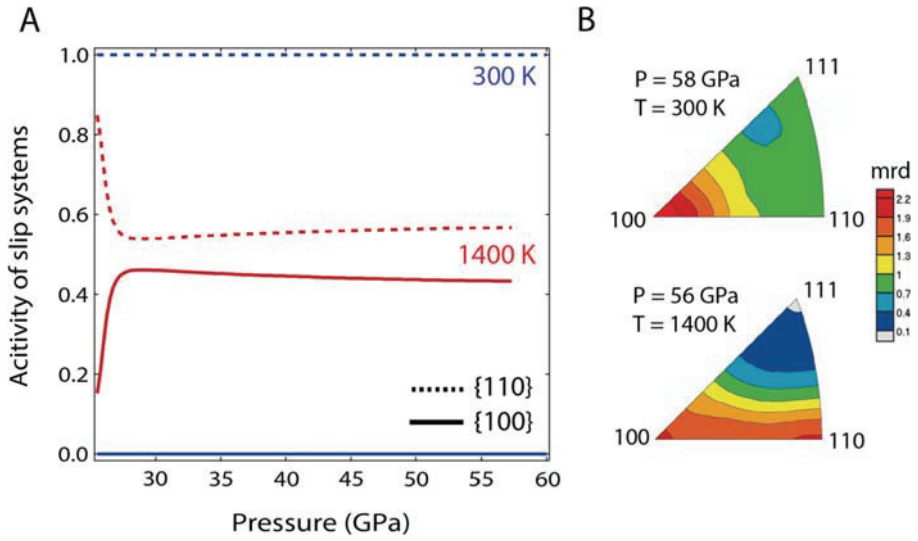

Fig. 3. Results of EVPSC modeling of the experimental data. (A) Pressure–temperature-dependence of relative slip system activities inferred from modeling the experiments at 1400 K (red) and 300 K (blue). (B) Modeled IPFs of the compression direction at high-P/T. Activity of {100}<011> slip leads to a shift of intensity maximum to 110 in the IPF. Mrd: multiples of random distribution.

and Wenk, 2016) and single crystal elastic constants (Wentzcovitch et al., 2004). In this model slip on (001) planes in multiple slip directions accounts for 72% of strain with the remaining 28% evenly distributed on (100) and (010) planes.

3. Results and discussion

Texture development represented by inverse pole figures (IPF) of the compression direction as derived from this work and our previous experiments at 300 K (Marquardt and Miyagi, 2015) is summarized in Fig. 2. Experimental runs at 300 K, 800 K, and 1150 K are characterized by the development of a strong 100 maximum upon initial pressure increase. At experimental tem-

Table 2
Parameters employed for EVPSC modeling of experimental data collected at 1400 K.

Slip system	τ_0 (GPa)	$d\tau/dP$	$d^2\tau/dP^2$ (GPa^{-1})	n
{110}<1$\bar{1}$0>	0.7	0.03	−0.0003	5
{100}<011>	0.9	0.09	−0.0008	5
{111}<1$\bar{1}$0>	50	0	0	5

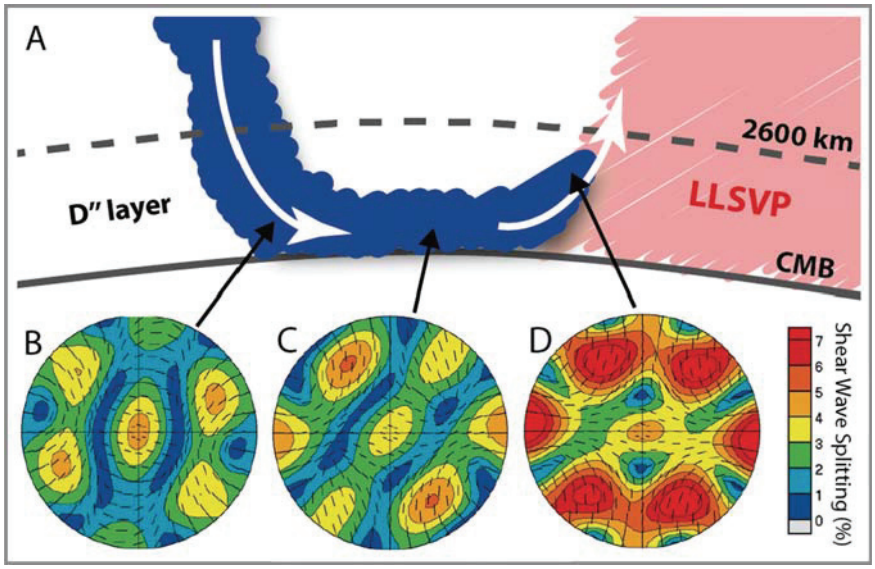

Fig. 4. Modeled seismic shear wave splitting from ferropericlase at three positions along a slab in the lowermost mantle (supplementary information). (A) Simplified sketch of a subducting slab impinging on the core–mantle-boundary (CMB) and entrained into upwelling at the margin of a Large Low Shear Velocity Province (LLSVP). Stereographic representation of calculated shear wave splitting predicted for ferropericlase where the slab approaches the CMB (B), after moving parallel to the CMB (C), and during upwelling (D). The CMB is horizontal and lines indicate the direction of fast shear wave polarization. The magnitude of predicted shear wave splitting in percent is color-coded. The presented shear wave splitting likely represents a lower bound as, in our calculation, only 10% of deformation is accommodated by dislocation movement. The corresponding elastic tensors as derived from VPSC are summarized in Table S3.

peratures of 300 K and 800 K, texture strength increases when pressure is increased, but the appearance of the IPF is generally unchanged (Fig. 2), similar to earlier deformation experiments conducted at room temperature on MgO (Merkel et al., 2002) and (Mg,Fe)O (Tommaseo et al., 2006; Lin et al., 2009; Marquardt and Miyagi, 2015). However, at 800 K we observe a tendency for the maximum to develop a shoulder towards 110 in the IPF. Deformation at higher temperature shows a different behavior. At pressures of about 30–40 GPa at 1150 K, a secondary texture maximum clearly develops at 110. At 1400 K, this maximum is present throughout the entire high-temperature compression in the experiment and gradually strengthens with pressure. According to recent theoretical work (Amodeo et al., 2016) and modeling based on experiments (Wang et al., 2010; Lin et al., 2017) (Fig. 3, supplementary information), the secondary maximum at 110 in the IPF is a clear indication for increased activity of {100}<011> slip.

Complementary modeling of both our experimental lattice strains and texture development using a recently developed Elasto-Visco-Plastic Self-Consistent code (EVPSC) allows us to extract slip system activities from our experimental data (Lin et al., 2017) as well as the corresponding absolute values of the slip systems' CRSS by comparing the experimental and simulated textures (Fig. S2) and lattice strains (Fig. S1). We note that it is difficult to model complex strain paths acquired prior to stabilization of the heater. For the measured lattice strains at 1400 K there is no data before ~25 GPa. Prior to 25 GPa the sample temperature was increased and the heater took time to stabilize. During this time there are fluctuations in temperature and pressure. This experimental difficulty leads to a complex strain and temperature history before the start of compression at 25 GPa, which cannot be modeled with EVPSC. Therefore, we focus on general trends, particularly the order and relative magnitude of experimental and modeled Q-factors as these are most relevant and most sensititve in determining the absolute CRSS values.

EVPSC modeling to reproduce published high-pressure data at 300 K (Marquardt and Miyagi, 2015) indicates 100% activity of slip on {110} throughout the entire experimental pressure range (Fig. 3). However, we find that at 1400 K and high pressures, slip on {110} and {100} contribute about equally to the overall deformation in our experiments, suggesting that slip on {100} becomes favorable with both pressure and temperature in the Earth's mantle.

Even though our conclusion is qualitatively consistent with most recent modeling results on single-crystal MgO (Amodeo et al., 2012; Cordier et al., 2012), our experimental data are not consistent with a full inversion of the easiest slip plane from {110} to {100} but rather a steady increase of {100} slip system activity. We note that the derived critical resolved shear stresses (CRSS) are difficult to compare directly to numerical models for single crystals. In the theoretical work, the CRSS are derived for single-crystal MgO, whereas the here-derived apparent CRSS are based on experimental data collected on polycrystalline samples. In polycrystalline materials, the strength and relative slip system activities differ from those inferred from the single-crystal CRSS, because they depend on additional effects, such as grain–grain-interactions, grain boundary processes, or back-stresses. This was confirmed by an additional test EVPSC simulation employing the predicted single-crystal CRSS for MgO (Amodeo et al., 2012) that did not reproduce the experimentally derived lattice strains. In particular, if the CRSS of {100} slip is set lower than that of {110} at a given pressure, the lattice strain parameters $Q(111)$ and $Q(220)$ will drop, which is not observed in the experiment.

4. Geophysical implications

Based on our findings, we expect a change in the dominant slip system activity to occur at conditions of the mid-lower mantle. Below the depths at which the slip system activity change, strain that builds up inside or in the vicinity of a subducting slab would be mostly accommodated by activity of {100}<011> slip if dislocation creep mechanisms operate. Between the mid-lower mantle and the lowermost mantle, a new type of CPO in ferropericlase would then progressively develop. In parallel, the elastic anisotropy of ferropericlase steadily increases with depth, particularly across the iron spin crossover (Marquardt et al., 2009). These processes can produce a continuous increase of seismic anisotropy of the mantle with depth that, in the lowermost mantle, may reach a threshold strength making it detectable for seismology (Fig. 4). It is worth noting that recent work indicates

the presence of anisotropy about 1000 km above the CMB and well above the D″ layer (de Wit and Trampert, 2015). However, as seismic studies mostly report seismic shear wave splitting in the lowermost mantle (Lay et al., 1998; Garnero et al., 2004; Panning and Romanowicz, 2004; Cottaar and Romanowicz, 2013; Lynner and Long, 2014; Romanowicz and Wenk, 2017), where seismic coverage is good, we restrict the following discussion to this region.

Paralleling previous work (Merkel et al., 2007; Miyagi et al., 2010), we use our results to model texture development in ferropericlase along a geodynamic streamline (Fig. 4, section 2.2) (McNamara and Zhong, 2005). We then combine the texture information with elasticity data to predict seismic shear wave splitting from deformed ferropericlase in the lower mantle, both in regions where sinking slabs impinge on the core–mantle boundary and in regions of upwellings. Here, the edges of Large Low Shear Velocity Provinces (LLSVP) seem of particular interest as previous work concluded that deformation is localized in these regions leading to detectable seismic anisotropy (Cottaar and Romanowicz, 2013; Lynner and Long, 2014; Garnero et al., 2016).

Our model shows that deformation of ferropericlase with dominant slip on {100} will produce a strong $V_{SH} > V_{SV}$ shear wave splitting for seismic waves propagating parallel to the CMB, i.e. horizontally polarized shear waves V_{SH} travel faster than vertically polarized shear waves V_{SV}, even if only 10% of the total deformation is accommodated by dislocation glide. Interestingly, the $V_{SH} > V_{SV}$ anisotropy produced by ferropericlase CPO is maintained along the entire geodynamic streamline, likely as a result of the high crystallographic symmetry of ferropericlase, and reaches a maximum in regions of upwellings (Fig. 4D). Based on our modeling, ∼20% of ferropericlase alone, as expected for a typical lower mantle, would be sufficient to produce 1–2% of seismic shear wave splitting as typically observed in the lowermost mantle (Lay et al., 1998; Garnero et al., 2004; Panning and Romanowicz, 2004; Cottaar and Romanowicz, 2013; Lynner and Long, 2014; Romanowicz and Wenk, 2017) (Fig. 4), at least for seismic ray paths along the slab. The predicted anisotropy was calculated for pure MgO for which complete datasets of elastic constants at high P/T are available unlike ferropericlase. As ferropericlase is elastically more anisotropic as compared to MgO (Marquardt et al., 2009), the predicted shear wave splitting likely represents a lower bound.

In addition to ferropericlase, post-perovskite and/or bridgmanite will contribute to measured seismic shear wave splitting. The deformation of post-perovskite, the dominant phase in cold regions of D″, might also result in a $V_{SH} > V_{SV}$ anisotropy pattern (Miyagi et al., 2010; Wu et al., 2017), thereby enhancing the contribution from ferropericlase. However, slip system activities in post-perovskite, including possible transformation textures, are still debated (Merkel et al., 2007; Miyagi et al., 2010; Dobson et al., 2013; Goryaeva et al., 2015; Wu et al., 2017), particularly as the experimental information on the high temperature behavior of post perovskite is extremely limited (Wu et al., 2017).

In hotter regions of the D″, such as upwellings, post-perovskite might become unstable due to the positive Clapeyron slope of the bridgmanite to post-perovskite phase transition (Murakami et al., 2004), stabilizing bridgmanite at high temperatures. Deformation of bridgmanite will result in $V_{SV} > V_{SH}$ shear wave splitting in regions of upwellings (Fig. S3) (Tsujino et al., 2016). Our results show that ferropericlase, instead, produces a strong $V_{SH} > V_{SV}$ shear wave splitting in these regions (Fig. 4D).

The magnitude of $V_{SH} > V_{SV}$ seismic shear wave splitting predicted from our model for ferropericlase, however, strongly depends on the raypath of the probing seismic wave. The strongest shear wave splitting (up to 7%) is observed for seismic waves propagating along the direction of slab movement, whereas other directions show little shear wave splitting (Fig. 4D). Moreover, for seismic waves that travel with some angle to the CMB, the pattern is more complicated and ferropericlase could produce a $V_{SV} > V_{SH}$ anisotropy, particularly in regions of upwelling.

Our model therefore predicts the character and magnitude of observed shear wave splitting, resulting from a combination of ferropericlase and bridgmanite CPO in upwellings to be highly sensitive to the probing seismic raypath. The observed complicated shear wave anisotropy distribution in the vicinity of the African Large Low Shear Velocity Province may thus be explained by competing anisotropy contributions from ferropericlase and bridgmanite CPO (Cottaar and Romanowicz, 2013; Lynner and Long, 2014; Romanowicz and Wenk, 2017).

The actual contributions of these two phases to D″ anisotropy will ultimately depend on the deformation behavior of a multiphase-assemblage at conditions of the lowermost mantle. Limited information from rotational Drickamer apparatus (Girard et al., 2016), diamond-anvil cell work at 300 K (Miyagi and Wenk, 2016), and experiments and modeling in analogue systems (Wang et al., 2013; Kaercher et al., 2016) indicate that strain heterogeneity on the grain scale may play a significant role for the rheological behavior of multiphase systems and the resulting CPO pattern. Possible changes in strain partitioning caused by temperature variations or strain (rate) may further complicate the resulting anisotropy pattern. Besides possible differences in CPO development in multiphase mixtures as compared to single-phase systems, a solid state shape preferred orientation (SPO) of ferropericlase and post-perovskite or bridgmanite may also contribute to generating seismic anisotropy. This would require SPO to develop and a large elastic contrast between the two phases. Also, aligned melt pockets could in principle contribute to the observed seismic anisotropy (Kendall and Silver, 1996). Despite these open questions, our results provide direct experimental proof for {100}<110> slip in ferropericlase at conditions of the lower mantle and demonstrate that ferropericlase may play an important role in generating seismic shear wave splitting in the lowermost mantle.

Acknowledgements

This research was supported through the projects “GeoMaX” funded under the Emmy-Noether Program of the German Science Foundation (MA4534/3-1) as well as grant MA4534/4-1. HM acknowledges support from the Bavarian Academy of Sciences. LM acknowledges support from CDAC and NSF (EAR-0337006 and EAR-1654687). SM acknowledges support from the Institut Universitaire de France and the program PNP of CNRS/INSU. We thank D. Frost for providing the ferropericlase powders and Konstantin Glazyrin for assistance at the ECB. We further acknowledge technical assistance by A. Ehnes and I. Schwark (Infrastructure for Extreme Conditions Research ECSI, DESY).

Appendix A. Supplementary material

Supplementary material related to this article can be found online at https://doi.org/10.1016/j.epsl.2018.02.045.

References

Amodeo, J., Carrez, P., Cordier, P., 2012. Modelling the effect of pressure on the critical shear stress of MgO single crystals. Philos. Mag. 92 (12), 1523–1541.
Amodeo, J., Dancette, S., Delannay, L., 2016. Atomistically-informed crystal plasticity in MgO polycrystals under pressure. Int. J. Plast. 82, 177–191.
Carrez, P., Ferré, D., Cordier, P., 2009. Peierls–Nabarro modelling of dislocations in MgO from ambient pressure to 100 GPa. Model. Simul. Mater. Sci. Eng. 17 (3), 035010.
Cordier, P., Amodeo, J., Carrez, P., 2012. Modelling the rheology of MgO under Earth/'s mantle pressure, temperature and strain rates. Nature 481 (7380), 177–180.

Cottaar, S., Li, M., McNamara, A.K., Romanowicz, B., Wenk, H.-R., 2014. Synthetic seismic anisotropy models within a slab impinging on the core–mantle boundary. Geophys. J. Int. 199 (1), 164–177.
Cottaar, S., Romanowicz, B., 2013. Observations of changing anisotropy across the southern margin of the African LLSVP. Geophys. J. Int. 195 (2), 1184–1195.
de Wit, R.W.L., Trampert, J., 2015. Robust constraints on average radial lower mantle anisotropy and consequences for composition and texture. Earth Planet. Sci. Lett. 429, 101–109.
Dobson, D.P., Miyajima, N., Nestola, F., Alvaro, M., Casati, N., Liebske, C., Wood, I.G., Walker, A.M., 2013. Strong inheritance of texture between perovskite and post-perovskite in the D″ layer. Nat. Geosci. 6 (7), 575–578.
Garnero, E.J., Maupin, V., Lay, T., Fouch, M.J., 2004. Variable azimuthal anisotropy in Earth's lowermost mantle. Science 306 (5694), 259–261.
Garnero, E.J., McNamara, A.K., Shim, S.-H., 2016. Continent-sized anomalous zones with low seismic velocity at the base of Earth's mantle. Nat. Geosci. 9 (7), 481–489.
Girard, J., Amulele, G., Farla, R., Mohiuddin, A., Karato, S.-i., 2016. Shear deformation of bridgmanite and magnesiowüstite aggregates at lower mantle conditions. Science 351 (6269), 144–147.
Girard, J., Chen, J., Raterron, P., 2012. Deformation of periclase single crystals at high pressure and temperature: quantification of the effect of pressure on slip-system activities. J. Appl. Phys. 111 (11), 112605–112607.
Goryaeva, A.M., Carrez, P., Cordier, P., 2015. Modeling defects and plasticity in $MgSiO_3$ post-perovskite, part 2: screw and edge [100] dislocations. Phys. Chem. Miner. 42 (10), 793–803.
Kaercher, P., Miyagi, L., Kanitpanyacharoen, W., Zepeda-Alarcon, E., Wang, Y., Parkinson, D., Lebensohn, R.A., De Carlo, F., Wenk, H.R., 2016. Two-phase deformation of lower mantle mineral analogs. Earth Planet. Sci. Lett. 456, 134–145.
Karato, S., 1998. Some remarks on the origin of seismic anisotropy in the D″ layer. Earth Planets Space 50, 1019–1028.
Karki, B.B., Wentzcovitch, R.M., de Gironcoli, S., Baroni, S., 1999. First-principles determination of elastic anisotropy and wave velocities of MgO at lower mantle conditions. Science 286 (5445), 1705–1707.
Kendall, J.M., Silver, P.G., 1996. Constraints from seismic anisotropy on the nature of the lowermost mantle. Nature 381 (6581), 409–412.
Lay, T., Williams, Q., Garnero, E.J., 1998. The core–mantle boundary layer and deep Earth dynamics. Nature 392 (6675), 461–468.
Lebensohn, R., Tomé, C., 1994. A self-consistent viscoplastic model: prediction of rolling textures of anisotropic polycrystals. Mater. Sci. Eng. A 175, 71–82.
Liermann, H.-P., Konopkova, Z., Morgenroth, W., Glazyrin, K., Bednarcik, J., McBride, E.E., Petitgirard, S., Delitz, J.T., Wendt, M., Bican, Y., Ehnes, A., Schwark, I., Rothkirch, A., Tischer, M., Heuer, J., Schulte-Schrepping, H., Kracht, T., Franz, H., 2015. The extreme conditions beamline P02.2 and the extreme conditions science infrastructure at PETRA III. J. Synchrotron Radiat. 22 (4), 908–924.
Liermann, H.-P., Merkel, S., Miyagi, L., Wenk, H.-R., Shen, G., Cynn, H., Evans, W.J., 2009. Experimental method for in situ determination of material textures at simultaneous high pressure and high temperature by means of radial diffraction in the diamond anvil cell. Rev. Sci. Instrum. 80 (10), 104501.
Lin, F., Hilairet, N., Ratteron, P., Addad, A., Immoor, J., Marquardt, H., Tomé, C., Miyagi, L., Merkel, S., 2017. Elasto-Viscoplastic Self Consistent (EVPSC) modeling of the ambient temperature plastic behavior of periclase deformed up to 5.4 GPa. J. Appl. Phys. 122, 205902.
Lin, J.-F., Speziale, S., Mao, Z., Marquardt, H., 2013. Effects of the electronic spin transitions of iron in lower-mantle minerals: implications to deep-mantle geophysics and geochemistry. Rev. Geophys. 51 (2), 244–275.
Lin, J.-F., Wenk, H.-R., Voltolini, M., Speziale, S., Shu, J., Duffy, T., 2009. Deformation of lower-mantle ferropericlase (Mg,Fe)O across the electronic spin transition. Phys. Chem. Miner. 36 (10), 585–592.
Lutterotti, L., Matthies, S., Wenk, H.-R., Schultz, A.S., Richardson, J.W., 1997. Combined texture and structure analysis of deformed limestone from time-of-flight neutron diffraction spectra. J. Appl. Phys. 81 (2), 594–600.
Lynner, C., Long, M.D., 2014. Lowermost mantle anisotropy and deformation along the boundary of the African LLSVP. Geophys. Res. Lett. 41 (10), 3447–3454.
Marquardt, H., Miyagi, L., 2015. Slab stagnation in the shallow lower mantle linked to an increase in mantle viscosity. Nat. Geosci. 8 (4), 311–314.
Marquardt, H., Speziale, S., Reichmann, H.J., Frost, D.J., Schilling, F.R., Garnero, E.J., 2009. Elastic shear anisotropy of ferropericlase in Earth's lower mantle. Science 324 (5924), 224–226.
Matthies, S., Humbert, M., 1993. The realization of the concept of a geometric mean for calculating physical constants of polycrystalline materials. Phys. Status Solidi B 177 (2), K47–K50.
Matthies, S., Vinel, G.W., 1982. On the reproduction of the orientation distribution function of texturized samples from reduced pole figures using the conception of a conditional ghost correction. Phys. Status Solidi B 112 (2), K111–K114.
McNamara, A.K., Zhong, S., 2005. Thermochemical structures beneath Africa and the Pacific Ocean. Nature 437 (7062), 1136–1139.
Merkel, S., McNamara, A.K., Kubo, A., Speziale, S., Miyagi, L., Meng, Y., Duffy, T.S., Wenk, H.-R., 2007. Deformation of (Mg,Fe)SiO_3 post-perovskite and D″ anisotropy. Science 316 (5832), 1729–1732.
Merkel, S., Tomé, C., Wenk, H.-R., 2009. Modeling analysis of the influence of plasticity on high pressure deformation of HCP-Co. Phys. Rev. B 79 (6), 064110.
Merkel, S., Wenk, H.R., Shu, J., Shen, G., Gillet, P., Mao, H.-k., Hemley, R.J., 2002. Deformation of polycrystalline MgO at pressures of the lower mantle. J. Geophys. Res. 107 (B11), 2271.
Miyagi, L., Kanitpanyacharoen, W., Kaercher, P., Lee, K.K.M., Wenk, H.-R., 2010. Slip systems in $MgSiO_3$ post-perovskite: implications for D″ anisotropy. Science 329 (5999), 1639–1641.
Miyagi, L., Wenk, H.R., 2016. Texture development and slip systems in bridgmanite and bridgmanite + ferropericlase aggregates. Phys. Chem. Miner. 43 (8), 597–613.
Murakami, M., Hirose, K., Kawamura, K., Sata, N., Ohishi, Y., 2004. Post-perovskite phase transition in $MgSiO_3$. Science 304 (5672), 855–858.
Nowacki, A., Walker, A.M., Wookey, J., Kendall, J.M., 2013. Evaluating post-perovskite as a cause of D″ anisotropy in regions of palaeosubduction. Geophys. J. Int. 192 (3), 1085–1090.
Nowacki, A., Wookey, J., Kendall, J.M., 2011. New advances in using seismic anisotropy, mineral physics and geodynamics to understand deformation in the lowermost mantle. J. Geodyn. 52 (3–4), 205–228.
Panning, M., Romanowicz, B., 2004. Inferences on flow at the base of Earth's mantle based on seismic anisotropy. Science 303 (5656), 351–353.
Romanowicz, B., Wenk, H.-R., 2017. Anisotropy in the deep Earth. Phys. Earth Planet. Inter. 269, 58–90.
Singh, A.K., Balasingh, C., Mao, H.-k., Hemley, R.J., Shu, J., 1998. Analysis of lattice strains measured under nonhydrostatic pressure. J. Appl. Phys. 83 (12), 7567–7575.
Stixrude, L., Lithgow-Bertelloni, C., 2011. Thermodynamics of mantle minerals, II: phase equilibria. Geophys. J. Int. 184 (3), 1180–1213.
Stretton, I., Heidelbach, F., Mackwell, S., Langenhorst, F., 2001. Dislocation creep of magnesiowüstite ($Mg_{0.8}Fe_{0.2}O$). Earth Planet. Sci. Lett. 194 (1–2), 229–240.
Tommaseo, C., Devine, J., Merkel, S., Speziale, S., Wenk, H.-R., 2006. Texture development and elastic stresses in magnesiowüstite at high pressure. Phys. Chem. Miner. 33 (2), 84–97.
Tsujino, N., Nishihara, Y., Yamazaki, D., Seto, Y., Higo, Y., Takahashi, E., 2016. Mantle dynamics inferred from the crystallographic preferred orientation of bridgmanite. Nature 539 (7627), 81–84.
Walker, A.M., Dobson, D.P., Wookey, J., Nowacki, A., Forte, A.M., 2017. The anisotropic signal of topotaxy during phase transitions in D″. Phys. Earth Planet. Inter.
Walker, A.M., Forte, A.M., Wookey, J., Nowacki, A., Kendall, J.M., 2011. Elastic anisotropy of D″ predicted from global models of mantle flow. Geochem. Geophys. Geosyst. 12 (10), Q10006.
Wang, H., Wu, P.D., Tomé, C.N., Huang, Y., 2010. A finite strain elastic–viscoplastic self-consistent model for polycrystalline materials. J. Mech. Phys. Solids 58 (4), 594–612.
Wang, Y., Hilairet, N., Nishiyama, N., Yahata, N., Tsuchiya, T., Morard, G., Fiquet, G., 2013. High-pressure, high-temperature deformation of $CaGeO_3$ (perovskite) ± MgO aggregates: implications for multi-phase rheology of the lower mantle. Geochem. Geophys. Geosyst.
Wenk, H.-R., Cottaar, S., Tomé, C.N., McNamara, A., Romanowicz, B., 2011. Deformation in the lowermost mantle: from polycrystal plasticity to seismic anisotropy. Earth Planet. Sci. Lett. 306 (1–2), 33–45.
Wenk, H.R., Lutterotti, L., Kaercher, P., Kanitpanyacharoen, W., Miyagi, L., Vasin, R., 2014. Rietveld texture analysis from synchrotron diffraction images, II: complex multiphase materials and diamond anvil cell experiments. Powder Diffr. 29, 220–232.
Wenk, H.R., Speziale, S., McNamara, A.K., Garnero, E.J., 2006. Modeling lower mantle anisotropy development in a subducting slab. Earth Planet. Sci. Lett. 245 (1–2), 302–314.
Wentzcovitch, R.M., Karki, B.B., Cococcioni, M., de Gironcoli, S., 2004. Thermoelastic properties of $MgSiO_3$-perovskite: insights on the nature of the Earth's lower mantle. Phys. Rev. Lett. 92 (1), 018501.
Wu, X., Lin, J.-F., Kaercher, P., Mao, Z., Liu, J., Wenk, H.-R., Prakapenka, V.B., 2017. Seismic anisotropy of the D″ layer induced by (001) deformation of post-perovskite. Nat. Commun. 8, 14669.
Yamazaki, D., Yoshino, T., Matsuzaki, T., Katsura, T., Yoneda, A., 2009. Texture of (Mg,Fe)SiO_3 perovskite and ferro-periclase aggregate: implications for rheology of the lower mantle. Phys. Earth Planet. Inter. 174 (1–4), 138–144.